ACS Catalysis

pubs.acs.org/acscatalysis Research Article

Ultrathin Silicon Oxide Overlayers Enable Selective Oxygen Evolution from Acidic and Unbuffered pH-Neutral Seawater

Amar A. Bhardwaj, Johannes G. Vos, Marissa E. S. Beatty, Amanda F. Baxter, Marc T. M. Koper, Ngai Yin Yip, and Daniel V. Esposito*

Cite This: ACS Catal. 2021, 11, 1316–1330 Read Online

ACCESS | Metrics & More | Article Recommendations | Supporting Information

ABSTRACT: Seawater electrolysis is an attractive approach for producing clean hydrogen fuel in scenarios where freshwater is scarce and renewable electricity is abundant. However, chloride ions (Cl^-) in seawater can accelerate electrode corrosion and participate in the undesirable chlorine evolution reaction (CER). This problem is especially acute in acidic conditions that naturally arise at the anode as a result of the desired oxygen evolution reaction (OER). Herein, we demonstrate that ultrathin silicon oxide (SiO_x) overlayers on model platinum anodes are highly effective at suppressing the CER in the presence of 0.6 M Cl^- in both acidic and unbuffered pH-neutral electrolytes by blocking the transport of Cl^- to the catalytically active buried interface while allowing the desired oxygen evolution reaction (OER) to occur there. The permeability of Cl^- in SiO_x overlayers is 3 orders of magnitude less than that of Cl^- in a conventional salt-selective membrane used in reverse osmosis desalination. The overlayers also exhibit robust stability over 12 h in chronoamperometry tests at moderate overpotentials. SiO_x overlayers demonstrate a promising step toward achieving selective and stable seawater electrolysis without the need to adjust the pH of the electrolyte.

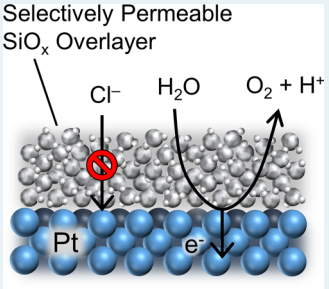

KEYWORDS: *seawater electrolysis, oxygen evolution reaction, chlorine evolution reaction, membrane-coated electrocatalysts, hydrogen, silicon oxide, coatings*

1. INTRODUCTION

"Green" hydrogen produced from water electrolysis powered by renewable electricity is a valuable zero emission energy carrier that could serve as an energy storage medium for intermittent renewable energy, a clean fuel in the transportation sector, or a feedstock for the chemical industry.[1−4] Producing green hydrogen by directly splitting abundant seawater instead of freshwater avoids competition for freshwater in locations and applications where freshwater is scarce[5] and avoids the need for costly desalination of seawater.[6] However, a major challenge to seawater electrolysis is that chloride ions, the predominant anion in seawater, participate in unfavorable side reactions at the anode that are in competition with the desired oxygen evolution reaction (OER, eq 1). In acidic conditions, chloride ions can combine to form chlorine (Cl_2) through the chlorine evolution reaction (CER, eq 2), while hypochlorite (OCl^-) is believed to be produced according to eq 3 in alkaline conditions[7]

$$2H_2O \rightarrow O_2 + 4H^+ + 4e^-;\ E^0 = 1.23\ \text{V vs RHE} \quad (1)$$

$$2Cl^- \rightarrow Cl_2 + 2e^-;\ E^0 = (1.36 + 0.059\cdot\text{pH})\ \text{V vs RHE} \quad (2)$$

$$Cl^- + 2\ OH^- \rightarrow ClO^- + H_2O + 2e^-;\ E^0 = 1.71\ \text{V vs RHE} \quad (3)$$

Although Cl_2 and OCl^- have commercial value, global demand for hydrogen is projected to reach over 40 times the demand for chlorine on a mole basis by 2024.[8−10] Producing H_2 at scale from seawater electrolysis while generating equimolar quantities of Cl_2 at the anode would soon lead to Cl_2 generation in excess of demand for chlorine. The excess toxic chlorine produced would be exceedingly difficult to manage and dispose of. On the other hand, the production of O_2 at the anode during seawater electrolysis would not be subject to the same management difficulties as Cl_2.

To achieve truly sustainable, large-scale hydrogen production from direct seawater electrolysis, it is therefore critically important to develop electrocatalysts and electrolyzer systems that selectively evolve O_2 at the anode. Unfortunately, the kinetics of Cl^- oxidation tend to be more favorable than those for the OER, in part because Cl^- oxidation requires the transfer of two electrons, while the OER is a four-electron reaction.[11] The most common approach to enhance O_2/Cl_2 selectivity is to increase the pH of seawater to carry out alkaline seawater electrolysis,[3,5,7,12,13] which makes the stand-

Received: October 6, 2020
Revised: December 24, 2020
Published: January 12, 2021

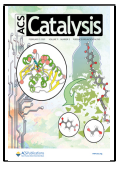

ard reduction potential for the OER ≈0.48 V more negative than that for OCl^- formation.[7] Thanks to this thermodynamic advantage and the abundance of stable and relatively active OER electrocatalysts in alkaline conditions, there have been many reports of OER faradic efficiencies (FEs) close to 100% during alkaline seawater electrolysis.[5,7,12−21] However, a major disadvantage of alkaline seawater electrolysis is that lye and fresh seawater must be continuously flushed through the electrolyzer to sustain an elevated pH and avoid producing concentrated brine, respectively.[22,23] The consumption of lye, as well as acid to neutralize the effluent stream, adds unwanted complexity, energy use, and cost to the system.[24] Furthermore, alkaline seawater electrolysis still faces the challenge of local acidification at the anode caused by the OER at very high current densities, which will eventually lead to the CER and/or stability issues.[25−27]

As an alternative to alkaline seawater electrolysis, the direct electrolysis of seawater at near-neutral pH could avoid the drawbacks associated with adding lye to the electrolyzer system. A pH-neutral environment is also more favorable for hybrid biological/electrochemical systems containing bacteria that cannot survive at the pH extremes typically encountered in water electrolysis.[28,29] A central challenge of realizing pH-neutral seawater electrolysis is that the oxidation of H_2O according to eq 1 coproduces H^+ ions, creating locally acidic conditions at the anode. This shifts the reversible potential for the OER closer to that for the CER while placing significant constraints on material options due to the lack of acid-stable OER catalysts that can operate at elevated current densities for significant periods of time.[30−34] To address these challenges, researchers often add pH buffers to maintain the electrolyte at a pH of 7 or above.[35−38] However, this entails continually adding buffer species to the electrolysis solution, and buffers may not be able to prevent large pH changes from occurring at the electrode−electrolyte interface at high OER current densities.[27,39] Further, unprotected electrocatalysts exposed to seawater of any pH are susceptible to corrosion from chlorine-based ions and molecules.[40] This challenge motivates exploration of solutions that go beyond engineering the pH of the electrolyte.

Recent studies have shown that rational control of species transport, rather than chemical kinetics, offers a promising approach to tune electrocatalyst selectivity for the desired reaction.[41,42] Overlayers composed of various semipermeable materials have been coated onto OER electrocatalysts to selectively reject the transport of chloride ions to the buried interface between the catalyst and overlayer while allowing diffusion of H_2O to the buried interface,[12,13,32−34,43−45] a necessity for the OER. The semipermeable overlayer in these encapsulated electrocatalysts thus provides selectivity for the OER over the CER and also offers the potential to block chloride-induced corrosion of the underlying OER electrocatalyst or chloride-induced leaching of OER catalyst material.[46−48]

However, previously reported overlayers have not demonstrated high OER selectivity and robust stability in the highly acidic environment created at the catalyst surface during the OER. In one notable study, semipermeable manganese oxide (MnO_x) overlayers deposited onto IrO_x anode catalysts were shown to enable high transport-based selectivity for the OER over the CER in weakly acidic conditions.[43] Although MnO_x is not thermodynamically stable in acidic conditions at potentials typically used for the OER, MnO_x-based OER electrocatalysts can be functionally stable due to a "self-healing" mechanism, whereby MnO_x is continuously regenerated on the anode through oxidation of dissolved Mn ions.[43,49] However, MnO_x is not functionally stable at the extremely low local pH conditions that may arise at the electrode during the OER at high current densities.[49,50] Additionally, the need to flow electrolyte through the electrolyzer is likely to lead to long-term degradation of ultrathin MnO_x coatings as dissolved Mn ions are gradually swept away from the electrode.

In this study, ultrathin semipermeable overlayers of silicon oxide (SiO_x) were investigated as alternative electrocatalyst coatings for selectively rejecting chloride ion transport in acidic and unbuffered pH-neutral solutions (Figure 1). Nanoscale

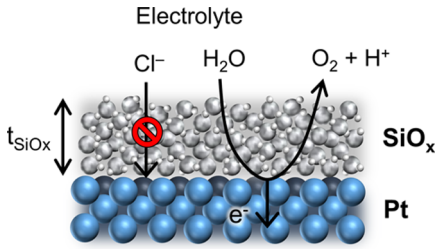

Figure 1. Schematic showing the planar SiO_x-encapsulated Pt thin film electrode capable of selectively blocking the undesired chlorine evolution reaction while permitting the desired oxygen evolution reaction to occur at the catalytic buried interface.

SiO_x films have previously been shown to function as highly selective "nanomembranes", including for SiO_x-modified gas-diffusion membranes,[51] and in electrocatalytic applications where they have been coated onto electrodes.[52−54] Further, silicon oxide is thermodynamically stable across a wide range of potentials in acidic and pH-neutral conditions[55] and is generally considered to be a catalytically inert material that will not promote reactions on its outer interface where it contacts the chloride-containing bulk electrolyte.

SiO_x overlayers investigated in this work were deposited onto well-defined Pt thin film electrocatalysts using a room-temperature photochemical process in which a poly(dimethylsiloxane) (PDMS) precursor was spin-coated onto the electrocatalyst surface and then converted to SiO_x by exposure to UV-generated ozone. By varying the initial PDMS concentration, this method affords nanometer-level control of overlayer thickness and produces continuous SiO_x films of uniform thickness that are characterized by surface root mean square (rms) roughness values less than 1 nm.[52] The density of the overlayers has been estimated to be 2.56 g cm^{-3}, corresponding to a free volume fraction of 3.3% if the filled volume elements of the SiO_x are assumed to have an identical density to void-free α-quartz.[56] SiO_x overlayers do not possess well-defined pores spanning the thickness of the film, but instead contain less ordered, sub-nanometer-sized free volume elements.[53] Pt was chosen as the active catalyst material because of its high activity for the CER and relatively poor activity for the OER, making it an ideal platform for easily deconvoluting OER and CER currents in voltammograms thanks to the significant differences in the OER and CER onset potentials.

Using these model SiO_x-encapsulated Pt electrodes (SiO_x|Pt), we show that nanoscopic SiO_x overlayers are highly effective at blocking Cl^- from reaching the electrocatalytic buried interface, markedly suppressing the CER at over-

https://dx.doi.org/10.1021/acscatal.0c04343
ACS Catal. 2021, 11, 1316−1330

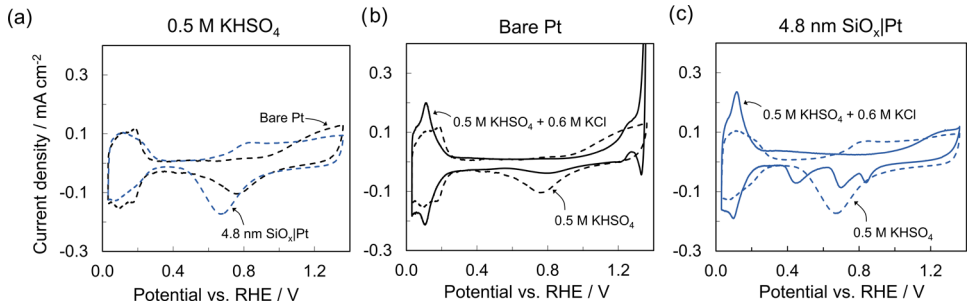

Figure 2. CV measurements for (a) bare Pt (black curves) and 4.8 nm SiO_x|Pt (blue curves) in 0.5 M $KHSO_4$. CV measurements for (b) bare Pt and (c) 4.8 nm SiO_x|Pt in 0.5 M $KHSO_4$ (dashed curves) and 0.5 M $KHSO_4$ + 0.6 M KCl (solid curves). All measurements were performed at 100 mV s^{-1} in deaerated electrolyte at pH 0.8 and 25 °C.

potentials exceeding 500 mV while still permitting for the desirable OER to occur. The overlayers greatly improve catalyst selectivity for the OER in unbuffered pH-neutral and acidic seawater conditions and show potential to protect the catalyst from chlorine corrosion. We further demonstrate the robust stability of the SiO_x overlayers under prolonged operation in acidic conditions and at large overpotentials. The possible mechanisms of selective transport through the overlayers are also discussed.

2. RESULTS AND DISCUSSION

2.1. Cyclic Voltammetry (CV) of SiO_x|Pt Electrodes.

The electrochemical characteristics of the as-made SiO_x|Pt electrodes were first evaluated by conducting cyclic voltammetry (CV) in a 0.5 M $KHSO_4$ (pH = 0.8) supporting electrolyte (Figure 2a). The oxidation and reduction peaks located between 0.0 and 0.3 V vs reversible hydrogen electrode (RHE) arise from hydrogen underpotential deposition (H_{upd}) and can be integrated to determine the electrochemically active surface area (ECSA) of the electrodes. Consistent with our previous studies of SiO_x-encapsulated Pt thin films,[52−54] the integrated H_{upd} signal for the 4.8 nm SiO_x|Pt electrode is only 4% less than that of bare Pt, suggesting that the Pt surface at the buried interface between Pt and SiO_x is still catalytically active and accessible to protons for H_{upd} by diffusion through the overlayer. Although the total integrated H_{upd} signals for the two samples are similar, the H_{upd} features for the 4.8 nm SiO_x|Pt electrode exhibit slight differences in shape and extend roughly 40 mV more positive than those for the bare Pt.

As the applied potential is swept from the H_{upd} region to more positive potentials, oxidation current is observed that is associated with Pt oxidation to platinum hydroxides and oxides (PtO_x). After reversing scan directions at the positive vertex, this PtO_x is subsequently reduced back to metallic Pt. Similar to previous reports,[52,54,57] the onset potential for PtO_x formation is shifted negative by ≈180 mV for the SiO_x-encapsulated sample compared to that for bare Pt. We attribute this shift in the PtO_x onset potential, as well as the aforementioned shift in the H_{upd} peaks, to the ability of the SiO_x overlayers to block bisulfate ions (HSO_4^-) from interacting with the buried interface. HSO_4^- ions are known to adsorb competitively onto Pt at potentials negative of the OH/O species adsorption that marks the first step of Pt oxidation, thereby inhibiting this step and shifting the PtO_x formation onset potential to more positive potentials.[58−60] This positive shift is clearly observed for bare Pt but is absent from the 4.8 nm SiO_x|Pt electrode, for which the Pt oxidation onset potential of 0.6 V vs RHE is consistent with that typically observed in aqueous acidic electrolytes lacking adsorbing counterions.[59] Similarly, the ability of SiO_x to block HSO_4^- may explain why the H_{upd} region of the SiO_x|Pt electrode extends to slightly more positive potentials than that for bare Pt, as HSO_4^- adsorption can compete with H^+ adsorption.

CV of bare Pt and 4.8 nm SiO_x|Pt electrodes were also carried out using identical scan conditions in a 0.6 M KCl solution containing the same 0.5 M $KHSO_4$ supporting electrolyte, where the KCl concentration was set to mimic the average chloride concentration found in natural seawater.[61] Though this 0.5 M $KHSO_4$ + 0.6 M KCl saline electrolyte has a higher ionic strength than the 0.5 M $KHSO_4$ supporting electrolyte, additional CV and linear sweep voltammetry (LSV) measurements for bare Pt in modified supporting electrolytes with the same ionic strength as the saline electrolyte show a minimal influence of ionic strength on the measurements (Figure S1). In Figure 2b,c, CV curves in 0.5 M $KHSO_4$ + 0.6 M KCl were superimposed on the CV curves in 0.5 M $KHSO_4$ for bare Pt and 4.8 nm SiO_x|Pt electrodes, respectively. Both samples exhibit substantial differences in CV characteristics in the 0.5 M $KHSO_4$ + 0.6 M KCl saline electrolyte. Most noticeable for the bare Pt electrode CV in Figure 2b is the appearance of a large oxidation peak associated with the CER close to the positive scan vertex. Concurrently, H_{upd} peaks on bare Pt are pushed to even more negative potentials, and the PtO_x peaks in both the positive and negative scan directions are significantly suppressed. Both of these changes can be attributed to Cl^- adsorption, with the latter being consistent with previous publications reporting that Cl^- adsorption suppresses Pt oxidation.[58,59,62]

As shown in the CV cycles in Figure 2c, the 4.8 nm SiO_x|Pt electrode responds very differently to the presence of chloride ions compared to bare Pt. Most significant is the observation that virtually no CER oxidation peak is seen at positive potentials up to 1.35 V, suggesting that the SiO_x overlayer might be blocking Cl^- from reaching the catalytic buried interface. However, comparison of the H_{upd} and PtO_x features to those recorded in the supporting electrolyte indicates that the SiO_x is not completely impermeable to Cl^-. As seen for the bare Pt electrode, the H_{upd} and Pt oxidation features for the 4.8 nm SiO_x|Pt electrode are also pushed to more negative and positive potentials, respectively, in the chloride-containing electrolyte.

Interestingly, the single PtO_x reduction peak on SiO_x|Pt that was centered at 0.68 V vs RHE in the supporting electrolyte is replaced in the saline electrolyte with three different PtO_x reduction peaks centered at 0.45, 0.70, and 0.84 V vs RHE. The evolution of these curves throughout the course of 19 CV

https://dx.doi.org/10.1021/acscatal.0c04343
ACS Catal. 2021, 11, 1316−1330

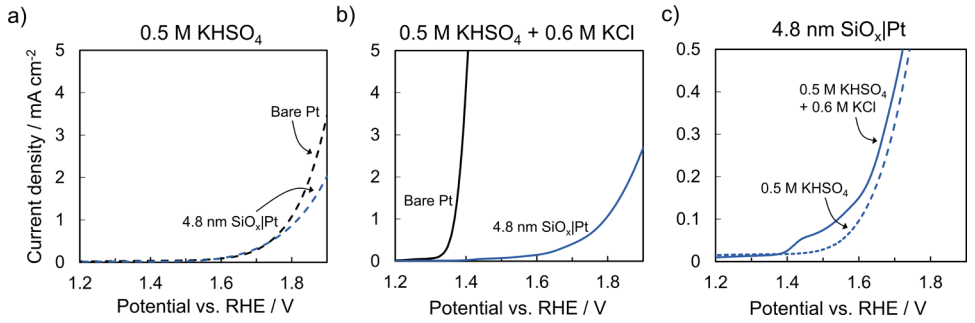

Figure 3. LSV measurements for bare Pt and SiO_x|Pt electrodes in (a) 0.5 M $KHSO_4$ and (b) 0.5 M $KHSO_4$ + 0.6 M KCl. (c) LSVs for 4.8 nm SiO_x|Pt in 0.5 M $KHSO_4$ and 0.5 M $KHSO_4$ + 0.6 M KCl (order-of-magnitude shorter vertical axis). All measurements were performed at 20 mV s^{-1} in deaerated electrolyte at pH 0.8 and 25 °C.

cycles on 4.8 nm SiO_x|Pt is provided in Figure S2. The first three CV cycles initiated immediately after immersion in the saline electrolyte show a PtO_x reduction peak consistent with the CV in the supporting electrolyte, indicating that Cl^- has not yet reached the buried Pt surface. The three distinct PtO_x reduction peaks appear in subsequent cycles in the order of the 0.70 V peak, followed by the 0.45 V peak, and finally the 0.84 V peak. The gradual appearance of the three PtO_x reduction peaks suggests that chloride ions slowly diffuse through the SiO_x overlayer upon the electrode's initial immersion, eventually reaching low concentrations at the buried interface after several cycles. We postulate that these chloride ions encounter, and are possibly blocked from, different nano-confined environments at the SiO_x|Pt interface, potentially associated with different Pt crystal facets or grain boundaries, which give rise to multiple distinct PtO_x reduction peaks.

The total integrated charge for PtO_x reduction decreases for the SiO_x|Pt electrode in the presence of Cl^- but to a lesser extent (≈55% decrease) than was observed for bare Pt in Figure 2b (≈75% decrease). These changes in PtO_x reduction charge in the presence of Cl^- can provide insight into the chloride concentration at the SiO_x|Pt buried interface. Novak and Conway[62] demonstrated a logarithmic relationship between the percentage of Pt oxide "blocked" during CV cycling due to competitive adsorption of Cl^- on a bare Pt electrode and the KCl concentration in the sulfuric acid electrolyte being used. According to this correlation, the 55% decrease in PtO_x reduction signal we observe for SiO_x|Pt corresponds to a ≈3 mM concentration of Cl^-, while the 75% decrease for bare Pt corresponds to ≈0.1 M Cl^-. This analysis suggests that while a small concentration of Cl^- reaches the buried Pt surface of SiO_x|Pt in the presence of a 0.6 M bulk chloride concentration, the selective SiO_x overlayer decreases the concentration of Cl^- at the buried interface by roughly 2 orders of magnitude compared to that of bare Pt under identical CV cycling conditions.

The greatly lowered chloride concentration at the buried interface of SiO_x|Pt mitigates, but does not eliminate, the risk of chloride-induced corrosion of the underlying electrocatalyst. Pt-, Ir-, Fe-, Ni-, and Co-based OER electrocatalysts are all known to be susceptible to dissolution in the presence of Cl^-.[48,63−66] Our analysis suggests that the SiO_x overlayer can decrease the chloride concentration at the buried electrocatalyst to millimolar levels in electrolytes containing 0.6 M Cl^-. This interfacial chloride concentration can be expected to drop to even lower values at mass transfer-limiting conditions for the CER. While some corrosion of OER electrocatalysts is still possible at millimolar chloride concentrations, corrosion will be significantly attenuated at these concentrations. By contrast, unencapsulated anodes composed of mixed metal oxides of Ni, Co, and Fe have demonstrated stability for up to days during OER operation in chloride concentrations of up to 4 M.[7,14,19,20,67] Importantly, the SiO_x overlayer may also help prevent leaching of metal cations produced by the dissolution of the electrocatalyst by blocking these cations' transport out from the buried interface. SiO_x overlayers have been previously shown to selectively reject aqueous Cu^{2+} ion transport,[53] and similar overlayer selectivity with other metal cations could minimize the rate of electrocatalyst corrosion. To further reduce the chloride concentration at the buried interface, anionic fixed charges could be incorporated into the SiO_x overlayer to electrostatically repel Cl^-. These considerations suggest that the risk of chloride corrosion of SiO_x-encapsulated anodes is manageable. Aside from its implications for corrosion, the indications of low chloride concentrations at the buried interface suggest that SiO_x|Pt may also suppress the CER, as discussed in the following section.

2.2. Evaluating Transport Properties of SiO_x Overlayers. To further investigate the ability of the overlayer to suppress the CER at more positive potentials relevant to the OER, linear sweep voltammetry (LSV) was performed in chloride-containing and chloride-free electrolytes under both unbuffered pH-neutral and acidic conditions. In the absence of chloride ions, the CER does not occur, allowing for an isolated view of OER activity. In the chloride-free supporting electrolyte at acidic pH (Figure 3a), the 4.8 nm SiO_x|Pt electrodes show an onset potential for the OER of ≈1.6 V vs RHE, which is nearly identical to the OER onset for bare Pt. Some suppression of the OER signal is seen for the SiO_x-encapsulated electrodes, which becomes more pronounced as the SiO_x thickness increases (Figure S3a). In the presence of 0.6 M KCl at low pH (Figure 3b), bare Pt shows a CER onset potential located 270 mV more negative than the OER onset potential seen in the supporting electrolyte, reaching a maximum total current density of ≈ 160 mA cm^{-2} at the vertex potential of 1.90 V vs RHE (Figure S4). Under the same conditions, SiO_x|Pt exhibits dramatically suppressed CER activity, maintaining current densities below 0.15 mA cm^{-2} at potentials negative of the OER onset identified in Figure 3a. For SiO_x|Pt in the saline electrolyte, the increase in current density recorded positive of the OER onset potential closely mirrors the OER behavior of SiO_x|Pt in the supporting electrolyte. This is confirmed by closer inspection of the low current density region of the overlaid LSV curves for the 4.8 nm SiO_x|Pt LSV curves in the supporting and saline electrolytes, which are provided in Figure 3c.

https://dx.doi.org/10.1021/acscatal.0c04343
ACS Catal. 2021, 11, 1316−1330

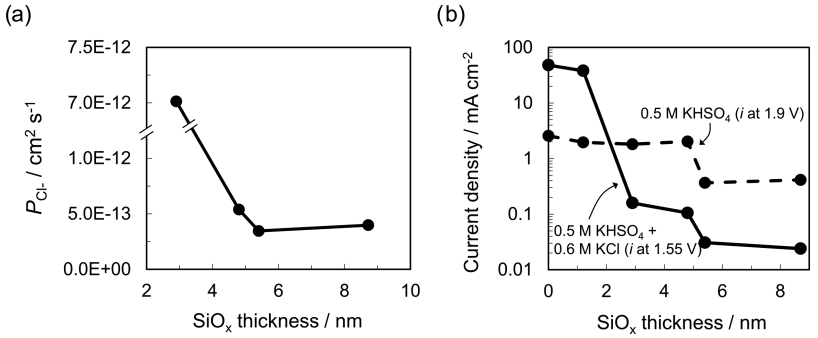

Figure 4. (a) Permeability of Cl^- in SiO_x overlayers as a function of overlayer thickness, calculated from LSVs for SiO_x|Pt in 0.5 M $KHSO_4$ + 0.6 M KCl using eq 4. (b) Current densities for SiO_x|Pt recorded at +1.90 V vs RHE during LSVs in 0.5 M $KHSO_4$ (dashed curve) and recorded at +1.55 V vs RHE during LSVs in 0.5 M $KHSO_4$ + 0.6 M KCl (solid curve).

The LSV curves in Figure 3c indicate that most of the oxidation current observed for the 4.8 nm SiO_x|Pt electrode in the saline electrolyte at potentials more positive than 1.6 V vs RHE is contributed by the OER rather than the CER. The enlarged view provided by the order-of-magnitude shorter vertical axis in Figure 3c reveals slightly elevated current densities compared to those measured in the supporting electrolyte, indicating that a very small amount of the CER still takes place on 4.8 nm SiO_x|Pt. Thanks to the large disparity in the OER and CER onset potentials, the difference curve between the chloride-containing and chloride-free LSVs for 4.8 nm SiO_x|Pt (Figure S5) clearly reveals the presence of a low mass transfer-limiting CER current density of ≈0.05 mA cm^{-2} at potentials negative of 1.60 V vs RHE without interference from the OER.

Assuming that Cl^- transport occurs only by diffusion through a continuous and uniform SiO_x overlayer to a planar Pt electrode, Faraday's law and Fick's law can be used to describe the steady-state flux of Cl^- to the electrode surface at mass transfer-limiting conditions for each SiO_x thickness. These equations relate the limiting current densities at steady state (i_{lim}) to the concentration of chloride ions at the interface between the SiO_x overlayer and the bulk electrolyte ($C_{Cl^-}(x = t_0)$), and the chloride permeability (P_{Cl^-}) within the overlayer (eq 4)

$$i_{lim,CER} = n \cdot F \cdot P_{Cl^-} \cdot \frac{C_{Cl^-}(x = t_0)}{t_0} \quad (4)$$

where n is the stoichiometric number of electrons, F is the Faraday constant, and t_0 is the thickness of the SiO_x overlayer. For large bulk chloride concentrations such as that used in this study, it can be assumed that the Cl^- concentration gradient across the bulk diffusion boundary layer is insignificant at low current densities, meaning that $C_{Cl^-}(x = t_0)$ is equal to the bulk chloride concentration. Based on the SiO_x thicknesses measured by ellipsometry and the CER limiting current densities observed in LSV measurements, eq 4 gives P_{Cl^-} values in the range of (3×10^{-13})–(6×10^{-13}) cm^2 s^{-1} for 4.8–8.7 nm thick SiO_x overlayers (Figure 4a). These values are 8 orders of magnitude lower than the bulk diffusivity of Cl^- in aqueous solutions[68] and 3 orders of magnitude lower than the permeability of Cl^- in aromatic polyamide,[69] a salt-selective membrane material used in reverse osmosis water desalination.

Nearly identical Cl^--blocking behavior is observed in LSV curves for 4.8 nm SiO_x|Pt recorded in unbuffered pH-neutral electrolyte with and without chloride ions (Figure S6). These LSVs show marked suppression of the CER in the presence of 0.6 M Cl^- and minimal suppression of the OER in the supporting electrolyte for 4.8 nm SiO_x|Pt compared to that for bare Pt at neutral pH, demonstrating the selectivity of the overlayer for the OER in unbuffered pH-neutral conditions in addition to acidic media.

These LSV curves demonstrating CER suppression on SiO_x|Pt are also reproducible in the acidic chloride-containing electrolyte that uses Na^+ as the cation instead of K^+ (Figure S7), relevant because Na^+ is the predominant cation in natural seawater. In an LSV in 0.5 M H_2SO_4 + 0.6 M NaCl, 4.8 nm SiO_x|Pt displays low current densities of ≈0.1 mA cm^{-2} at potentials negative of 1.6 V vs RHE due to CER suppression and increasing current densities positive of 1.6 V vs RHE due to the onset of the OER. In contrast, the bare Pt electrode in the Na^+-containing electrolyte shows a large CER current with an onset potential of 1.3 V vs RHE, mirroring our results for bare Pt in the K^+-containing electrolyte. The strong agreement between LSVs in the presence of K^+ and Na^+ suggests that our results using K^+ are applicable to electrolysis of Na^+-rich natural seawater.

Additional LSV curves using SiO_x overlayers of varied thickness in 0.5 M $KHSO_4$ and 0.5 M $KHSO_4$ + 0.6 M KCl (Figure S3) demonstrate that there is a narrow range of SiO_x thicknesses for which the CER signal is greatly suppressed without also substantially decreasing the OER signal. This is summarized in Figure 4b, which, as a function of overlayer thickness, plots the current density at 1.55 V vs RHE from LSVs in the acidic chloride solution as a measure of the ability of SiO_x to block Cl^- transport (solid curve) and the current density at 1.90 V vs RHE from LSVs in the supporting electrolyte as a measure of the ability to permit species transport associated with the OER (dashed curve). This figure shows that a SiO_x overlayer thickness of ≈3 nm or more is needed to suppress the CER, but making the overlayer much thicker than 4.8 nm also leads to a significant decrease in the desired OER current density.

The estimated faradic efficiency (FE) of SiO_x|Pt for the OER further illustrates the thickness-dependent performance of the SiO_x overlayers. The FE was estimated from saline LSVs by linearly extrapolating the CER mass transfer-limiting current region that appears negative of the OER onset and assuming all additional current arises from the OER. This method is depicted in Figure S8a, and the FE of 2.9–8.7 nm SiO_x|Pt as a function of potential is shown in Figure S8b; 4.8 nm SiO_x|Pt has the highest FE compared to thicker and thinner SiO_x overlayers for all potentials positive of 1.6 V vs RHE and reaches a maximum FE of 85% toward the OER at 1.90 V vs

https://dx.doi.org/10.1021/acscatal.0c04343
ACS Catal. 2021, 11, 1316–1330

RHE. The FE values of all SiO_x|Pt electrodes are greatly increased compared to that of bare Pt, which reaches a maximum FE of 1.6% at 1.90 V vs RHE, once again demonstrating the high selectivity of the SiO_x|Pt electrocatalysts for the OER over the CER.

The selectivity of the SiO_x overlayer for the OER over the CER is particularly notable considering the unfavorable conditions for the OER in this study, which involved a poor OER electrocatalyst (Pt) while using large Cl^- concentrations in an acidic environment. Compared to previous studies in acidic conditions that have used lower chloride concentrations,[31,43] the 0.6 M chloride concentration used here presents a significantly greater challenge to achieving high OER selectivity. Additionally, we expect that the application of Sio_x overlayers to more active OER electrocatalysts will allow for significant increases in OER faradic efficiencies over the same potential range studied here, for which Pt exhibits very low OER partial current densities. The FE of SiO_x|Pt for the OER should thus be viewed in the context of the combination of disadvantages overcome to achieve it.

In addition to rejecting Cl^-, the SiO_x overlayer must allow O_2 and H^+ to escape through the overlayer as they are evolved at the buried interface during the OER, to reduce OER concentration overpotentials. In a separate recent study from our group,[56] the O_2 and H^+ permeabilities (P_{O_2} and P_{H^+}) of SiO_x overlayers were determined from the mass transfer-limiting current densities associated with the oxygen reduction reaction (ORR) and hydrogen evolution reaction (HER), respectively. For SiO_x overlayers with comparable thicknesses and identical UV−ozone treatment to those used in this study, P_{O_2} and P_{H^+} were reported to be $(2.1 \pm 0.6) \times 10^{-9}$ and $(1.0 \pm 0.5) \times 10^{-7}$ cm^2 s^{-1}, respectively. These values are 4−6 orders of magnitude greater than the values of P_{Cl^-} found in this study, indicating that the overlayer does not suppress the transport of O_2 and H^+ to the same extent that it does for Cl^-. While the Pt electrocatalyst substrate used in these experiments was significantly thicker than that used herein, which has been known to cause changes to SiO_x overlayer permeabilities,[52] these changes are not expected to span orders of magnitude. The relatively high P_{O_2} and P_{H^+} of SiO_x overlayers will promote the transport of O_2 and H^+ away from the buried interface, helping to reduce OER concentration overpotentials. Higher values of P_{O_2} are also expected to be beneficial for mitigating the formation of O_2 gas nanobubbles at nanoscopic voids at the buried interface, where they could facilitate overlayer delamination. Due to the unfavorable energetics of O_2 nanobubble formation, dissolved O_2 concentrations orders of magnitude greater than the equilibrium O_2 saturation concentration may be required to nucleate nanobubbles.[70] Overlayers characterized by high P_{O_2} are expected to result in lower concentrations of dissolved O_2 within the overlayer, reducing the likelihood of nanobubble nucleation.

2.3. Stability of SiO_x|Pt Electrodes. In addition to characterizing the selective transport properties of SiO_x overlayers, the stability of SiO_x-encapsulated electrodes was investigated using chronoamperometry (CA) tests conducted at 1.55 and 1.90 V vs RHE in the 0.5 M $KHSO_4$ (+0.6 M KCl) electrolyte. A potential of 1.55 V vs RHE was chosen because it lies in between the CER and OER onset potentials seen for bare Pt in Figure 3a,b, respectively. Thus, CA measurements performed at 1.55 V vs RHE in low pH (Figure 5a,c) provide sufficient overpotential for the CER, but not the OER, to occur on Pt. An applied potential of 1.90 V vs RHE (Figure 5b,d) then provides a large enough overpotential for both reactions to occur on Pt.

CA curves measured at 1.55 V vs RHE in the chloride-free supporting electrolyte are provided in Figure 5a, where it is seen that the pseudo-steady-state current densities of both bare Pt and 4.8 nm SiO_x|Pt electrodes are well below 10 μA cm^{-2}. This result is consistent with the fact that there is little to no OER activity on the Pt electrodes at this potential. The very small oxidation currents that are observed likely result from Pt oxidation, where the growth of insoluble PtO_x at the Pt surface proceeds logarithmically in time but does not reach a saturation point under the conditions of this study.[52,58,59,71] Interestingly, the integrated charge passed by the bare Pt electrode after 30 min is 4 times greater than that for the 4.8 nm SiO_x|Pt electrode. Assuming that all of the current passed was associated with the oxidation of Pt, this finding suggests that the SiO_x overlayer serves as a sort of artificial passive oxide that helps to suppress Pt dissolution and/or limit the rate of PtO_x formation at the SiO_x|Pt buried interface. Further investigations are needed to test this hypothesis, but the proposed explanation is supported by our previous studies showing that SiO_x overlayers are effective diffusion barriers for Cu^{2+} ions.[52,53]

Upon increasing the applied potential to 1.90 V vs RHE in the supporting electrolyte (Figure 5b), the oxidation current densities increase by 1−2 orders of magnitude, which we attribute to the presence of the OER. After recording initial peak current densities of 7.4 and 1.0 mA cm^{-2} at the start of the CA measurements for bare Pt and 4.8 nm SiO_x|Pt, respectively, the current densities rapidly decrease over the first ≈1 h. Then, the current densities more gradually decrease over the remaining 11 h to final values of 0.07 and 0.02 mA cm^{-2} for bare Pt and 4.8 nm SiO_x|Pt, respectively. These observed decreases in current densities most likely result from the formation of the aforementioned PtO_x surface species, which are known to have lower catalytic activity for the OER and the CER compared to metallic Pt.[58,72,73]

When CA experiments were repeated for identical freshly prepared electrodes in the presence of 0.6 M KCl, the presence of the CER led to significant increases in current densities for CA tests at 1.55 V vs RHE (Figure 5c) and 1.90 V vs RHE (Figure 5d). After 12 h of operation, bare Pt held at 1.55 V vs RHE exhibits the largest pseudo-steady-state current density (≈10 mA cm^{-2}), while the 4.8 nm SiO_x|Pt electrode records the smallest current density (≈0.02 mA cm^{-2}). Further, the CA for the SiO_x|Pt electrode displays no increase in current density over 12 h of operation, highlighting the ability of the SiO_x overlayer to achieve a high degree of CER suppression over long time periods in high chloride concentrations and acidic environment.

In the saline electrolyte at 1.90 V vs RHE (Figure 5d), bare Pt shows substantial current density, although it is lower than current densities recorded at 1.55 V vs RHE. As previously reported, the decreased CER current on bare Pt at very positive potentials can be attributed to the increased growth of PtO_x surface species that inhibit CER kinetics.[58,72,73] By contrast, the CA curve for the 4.8 nm SiO_x|Pt electrode in the saline electrolyte at 1.90 V vs RHE shows an increased current density compared to that recorded in the chloride-free supporting electrolyte at 1.90 V vs RHE. This increase suggests that the CER is able to occur to a greater extent at

https://dx.doi.org/10.1021/acscatal.0c04343
ACS Catal. 2021, 11, 1316−1330

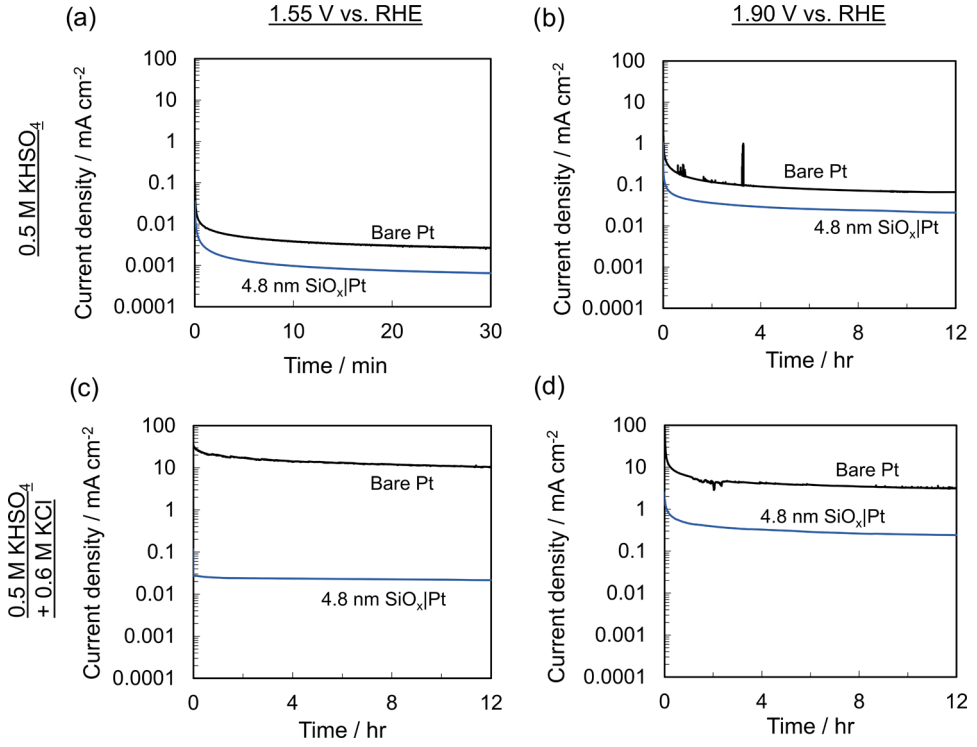

Figure 5. CA stability measurements for bare Pt and 4.8 nm SiO_x|Pt in 0.5 M $KHSO_4$ at constant applied potentials of (a) 1.55 V vs RHE and (b) 1.90 V vs RHE. 12 h CA stability measurements for bare Pt and 4.8 nm SiO_x|Pt in 0.5 M $KHSO_4$ + 0.6 M KCl at constant applied potentials of (c) 1.55 V vs RHE and (d) 1.90 V vs RHE. All measurements were performed in deaerated electrolyte at pH 0.8 and 25 °C.

1.90 V vs RHE than at 1.55 V vs RHE on SiO_x|Pt. However, the fact that the current density for SiO_x|Pt remains stable at more than an order of magnitude lower than that observed for the bare Pt electrode attests to the ability of the SiO_x overlayer to greatly suppress the CER even under large operating overpotentials (≈600 mV vs $E^0_{Cl^-/Cl_2}$).

While it is possible that the higher current density at 1.90 V could result from elevated Cl^- migration rates across the overlayer thanks to a higher electric field strength at the electrode−electrolyte interface, mechanical instability of the SiO_x overlayer may also be responsible. Some evidence for overlayer degradation/delamination is observed in the earliest portion of the 1.90 V vs RHE CA curve (Figure S9), where an initial gradual decay in current density is interrupted by a multistep increase in current from t = 12 to 54 s. While the current density then decreases gradually without similar interruptions beyond this point, the initial increase in current density yields a higher steady-state current density than would have otherwise occurred. The same feature is absent from the early time periods of the CA curves recorded at 1.55 and 1.90 V vs RHE in the supporting electrolyte.

To investigate the physical stability of the SiO_x overlayers, ellipsometry, X-ray photoelectron spectroscopy (XPS), and scanning electron microscopy (SEM) characterization measurements were performed on 4.8 nm SiO_x|Pt electrodes before and after the 12 h CA tests in the saline electrolyte. SEM images of the as-made SiO_x|Pt samples before each stability test show a smooth, continuous SiO_x surface with minimal defects (Figure 6a,b, left). After the 12 h CA test at 1.55 V vs RHE in the saline electrolyte (Figure 5c), SEM shows dark-colored micron-scale features covering a small fraction of the surface (Figure 6a, right), which we ascribe to debris accumulated on the sample during testing and handling. The SiO_x overlayer otherwise displays minimal degradation after the CA at 1.55 V vs RHE.

Importantly, XPS Si 2p spectra showed that SiO_x was still present on the electrode surface following the 12 h CAs in the saline electrolyte at both 1.55 and 1.90 V vs RHE (Figure 6c). The 4.8 nm SiO_x|Pt sample tested at 1.55 V vs RHE appears unchanged in SEM images taken post-CA (Figure 6a, right) and demonstrates only a 2% reduction in the atomic Si/Pt signal ratio as measured by XPS (Figure 6d), corroborating the overlayer's stability in this test. In contrast, the 4.8 nm SiO_x|Pt electrode characterized by SEM after the stability test at 1.90 V vs RHE displays cracking and delamination of the SiO_x overlayer (Figure 6b, right) and a 40% reduction in the atomic Si/Pt signal ratio (Figure 6d). While some of the damage to the SiO_x overlayer could have been incurred upon rinsing and drying of the sample after removal from the electrochemical test cell, it is likely that some degree of overlayer instability had already developed during the CA test and may explain the increased CER current for the 4.8 nm SiO_x|Pt electrode in the CA at 1.90 V vs RHE. We postulate that the overlayer's mechanical integrity was partially compromised 12 s into the CA, creating the aforementioned increase in current observed at that time in Figure S9. After this initial perturbation, the continuous decline in current density throughout the remainder of the CA suggests that further damage to the overlayer was limited.

Although additional experimentation is needed to confirm the origin of the damage caused to the 4.8 nm SiO_x overlayers during operation at 1.90 V vs RHE, it is likely that thicker PtO_x interlayers formed between Pt and SiO_x at such positive applied potentials could be a contributing factor. This interlayer-mediated degradation mechanism is supported by our prior study on SiO_x-encapsulated Pt thin films that found

https://dx.doi.org/10.1021/acscatal.0c04343
ACS Catal. 2021, 11, 1316−1330

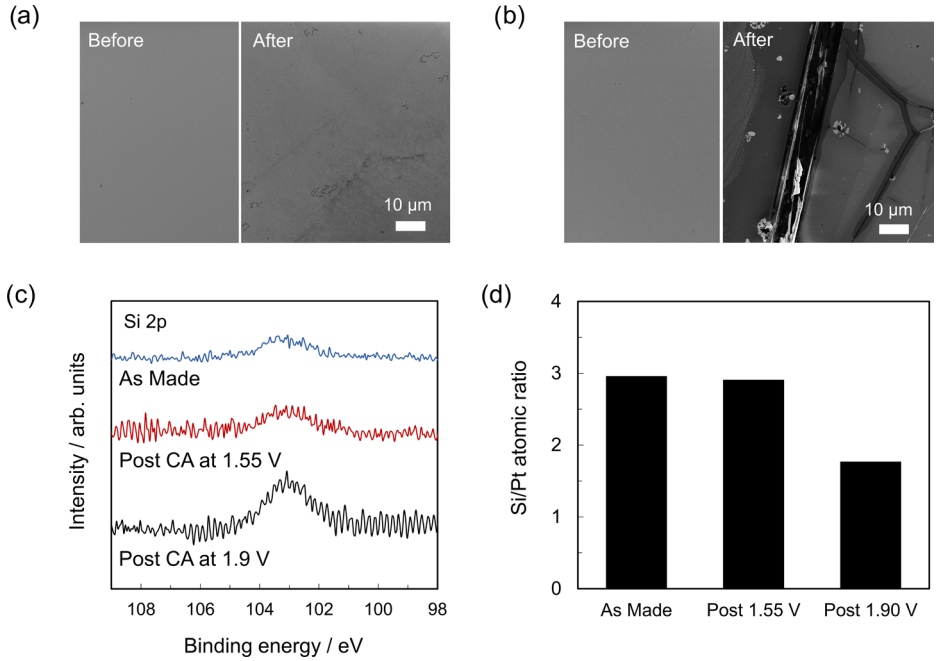

Figure 6. SEM images of 4.8 nm SiO_x|Pt before (left) and after (right) 12 h CA in 0.5 M $KHSO_4$ + 0.6 M KCl at (a) 1.55 V vs RHE and (b) 1.90 V vs RHE. (c) XPS Si 2p spectra for 4.8 nm SiO_x|Pt electrodes as-made and post-CA and (d) Si/Pt atomic ratio for as-made and post-CA samples. CAs performed in 0.5 M $KHSO_4$ + 0.6 M KCl electrolyte for a duration of 12 h. Potentials provided in the subfigures are given vs the RHE.

that SiO_x|Pt electrodes subjected to CV cycling over potential ranges extending to potentials more positive than the Pt oxidation onset potential exhibited accelerated delamination compared to those cycled over a narrow potential range that remained below the PtO_x onset potential.[52] Since PtO_x overlayers grow faster and to thicker values at more positive potentials,[58,73] and PtO_x is less dense than Pt, the formation and expansion of a thicker PtO_x interlayer at 1.90 V vs RHE could create more interfacial stress with the SiO_x overlayer, causing the cracking and partial delamination observed in Figure 6b. Since an increase in current density was observed at the outset of the CA at 1.90 V vs RHE in saline but not in the supporting electrolyte, it is possible that interactions between Cl^-/Cl_2 and SiO_x|Pt, or the higher current densities observed in the saline electrolyte, could play an additional role in SiO_x overlayer instability when operated at very positive applied potentials.

Despite the partial delamination observed during extended CA measurements at 1.90 V vs RHE, there are several reasons to remain optimistic that SiO_x overlayers can remain stable under industrially relevant conditions. First, the SiO_x overlayer shows no signs of degradation over 12 h at 1.55 V vs RHE in the acidic electrolyte with 0.6 M Cl^-. While the overlayer does exhibit some degradation at 1.90 V vs RHE, there is good reason to believe that this instability is associated with oxidation of the underlying Pt electrocatalyst rather than (electro)chemical instability of the overlayer itself. This degradation mechanism may be avoided through the use of active OER electrocatalysts that have strong adhesive interactions with SiO_x and are not susceptible to the formation of interlayers that can create detrimental interfacial stresses. Further, high-surface-area electrode designs based on supported electrocatalytic nanoparticles will contain catalytically inert support material to which SiO_x overlayers may become anchored without any stress-inducing OER chemistry occurring at the SiO_x|support interface. Takenaka et al. have shown that SiO_2-encapsulated Pt nanoparticles supported on high-surface-area carbon-based supports for the oxygen reduction reaction (ORR) can exhibit excellent durability over 20 000 cycles of CV,[74,75] a result that bodes well for the use of similar encapsulated electrocatalyst architectures for other applications like the OER.

2.4. Mechanisms of Selective Transport through SiO_x Overlayers. A deeper understanding of the transport mechanisms through amorphous silicon oxide overlayers is necessary to explain their ability to selectively block Cl^- ions and to guide the design of optimized SiO_x-encapsulated electrodes for seawater electrolysis. Several recent studies of SiO_x-encapsulated Pt electrodes have given insights into H^+ and O_2 transport through SiO_x overlayers,[41,56,76] but overall, little is known about the structure–property relationships of oxide-encapsulation layers that dictate trends in permeabilities across various types of electroactive species. To gain further insight into the origins of the low chloride permeability of SiO_x overlayers, we investigated the ability of SiO_x overlayers to similarly block Br^- ions as measured by monitoring the bromine evolution reaction (BER, eq 5)

$$2Br^- \rightarrow Br_2 + 2e^-;\ E^0 = 1.07\ \text{V vs NHE} \qquad (5)$$

The BER was selected for additional measurements because it is similar in many ways to the CER, with identical stoichiometry and similar standard reduction potentials, fast two-electron kinetics, and reactant species that are both monatomic, monovalent anions. The primary differences are that Br^- has a larger bare ion radius and lower hydration energy than Cl^-.[77−79] Thus, a comparison of chloride and bromide permeabilities determined from CER and BER measurements, respectively, can give insights into the importance of permeant size and/or hydration energy on species flux and transport mechanism(s). The permeability of Br^- (P_{Br^-}) through ≈5 nm thick SiO_x overlayers was determined from analysis of LSV curves measured with bare

https://dx.doi.org/10.1021/acscatal.0c04343
ACS Catal. 2021, 11, 1316−1330

Pt and 4.8 nm SiO_x|Pt in 0.5 M $KHSO_4$ + 20 mM KBr (Figure S10) to probe the BER on SiO_x-encapsulated electrodes. The calculation of P_{Br^-} followed the procedure described by Beatty et al.,[56] with an abbreviated description and list of equations included in Section XI, Supporting Information. Through this calculation, P_{Br^-} was determined to be 1.4×10^{-11} cm^2 s^{-1}. This value is roughly 2 orders of magnitude larger than the calculated P_{Cl^-} value of 5.4×10^{-13} cm^2 s^{-1} for 4.8 nm SiO_x|Pt, meaning that Br^- transport in the SiO_x overlayer is significantly faster than that of Cl^-.

Borrowing concepts from transport theory across dense films widely employed in synthetic membranes, there are several possible explanations for the large differences between P_{Br^-} and P_{Cl^-} that rely on understanding how a solute species interacts with the membrane or overlayer material and how those interactions depend on the structure and composition of both the membrane and solute. Here, we consider several different explanations, providing evidence and logic for and against each.

The first possible explanation is steric size exclusion on the basis of the hydrated radii of solute species, whereby a solute encounters a barrier to entering and traveling through the overlayer if its size nears or exceeds that of nanoscopic pores or free volume elements within the overlayer.[80−83] Previous characterization measurements of SiO_x overlayers made by the identical UV−ozone process used in this study have shown that they are amorphous, hydrophilic, and do not have well-defined pores spanning the thickness of the overlayer.[56,84] Thus, the ions likely travel through free volume elements in SiO_x where size exclusion may occur. Despite having a smaller bare ion radius, Cl^- has a hydrated radius that is very similar to that of Br^- because Cl^- has a higher charge density in its electron shell, creating a stronger electric field around the ion to coordinate water molecules.[85] Based on the nearly identical hydrated radii, it is unlikely that steric effects involving the hydrated ions can fully account for the 2-order-of-magnitude difference between P_{Br^-} and P_{Cl^-}. This is supported by previous studies investigating the selective transport of hydrated ions through membranes based on a size exclusion mechanism, which found that ions differing in hydrated radii by <0.1 Å typically exhibited less than a 2-fold difference in permeability values.[86,87] If the ions instead travel through the overlayer in a fully dehydrated state, a steric size exclusion mechanism is also unlikely because Br^- has a larger bare ion radius than Cl^-,[77] yet has a higher permeability in SiO_x.

Differences in electrostatic interactions between the solute and overlayer offer another possible explanation for the origin of $P_{Br^-} > P_{Cl^-}$. As ions partition into the overlayer, fixed charges within the overlayer can repel or attract solutes to varying degrees, giving rise to differences in species permeabilities.[80,88,89] In the transport of Cl^- and Br^- across a membrane with sub-nanometer pores and negative fixed charges, Epsztein et al. have found that Cl^- is repelled more strongly by the membrane's charges compared to Br^- due to the chloride's smaller bare ion radius and therefore higher charge density.[90] If the SiO_x overlayer contains negative fixed charges, these findings suggest that electrostatic repulsion would hinder the transport of Cl^- more strongly than that of Br^-, which is consistent with our result of $P_{Br^-} > P_{Cl^-}$. While SiO_x could contain negatively charged deprotonated silanol groups (Si−O^-), these groups would likely be protonated and neutrally or positively charged at our acidic electrolyte pH of 0.8, which is below the point of zero charge for silica that typically lies between 1 and 3.[91,92] In their study, Epsztein et al. reported that below the point of zero charge, the positively charged membrane electrostatically repels the counterions of Cl^- and Br^-, which in turn slows the transport of Cl^- and Br^- to maintain electroneutrality.[90] In our study at extremely low pH, the counterion for Cl^- and Br^- is likely H^+, which permeates through SiO_x in acidic conditions at a much faster rate than these anions,[56] and would not be expected to limit their transport. Thus, a purely electrostatic mechanism is unlikely to be the reason for the difference between our observed Cl^- and Br^- permeabilities.

A third possible explanation for the vastly different permeabilities of Cl^- and Br^- is that these ions must shed all or part of their hydration sphere to enter the SiO_x matrix and that the activation energies associated with dehydration are different. If the average dimension of the free volume elements in an overlayer or membrane is smaller than the size of the ion's hydration sphere, the hydration sphere must usually be removed or rearranged to allow the ion to partition into the membrane.[93,94] During dehydration, the rearrangement of the bonds between water molecules and the ion presents an energy barrier to transport.[95]

Whether or not it is a rate-limiting transport barrier, partial dehydration likely does occur during the transport of Cl^- and Br^- through SiO_x. Partial dehydration is often a prerequisite for achieving selective transport between two different ions in membranes because ion dehydration exposes the unique properties of each ion for the solute−medium interactions that give rise to selective transport.[95,96] Further, the polar bonds in SiO_x would likely form favorable interactions with the ions to displace ion−water interactions, promoting dehydration.[86,97] Saliently, partial dehydration has been found to be a key underlying reason for selective transport across a range of membrane materials.[83,94,98−104]

Recent characterization measurements reported by our group for SiO_x overlayers fabricated in an identical manner to those studied here provide further support that Br^- and Cl^- likely undergo partial dehydration to enter and diffuse through SiO_x. Based on ellipsometric porosimetry measurements carried out with toluene, Labrador et al. concluded that most of the free volume elements within SiO_x overlayers must have a diameter smaller than the kinetic diameter of toluene, 5.8 Å.[53] More recently, Beatty et al. used a combination of ellipsometry and XPS characterization to estimate the average nearest-neighbor Si−Si distances within 120 min cured 4.8 nm SiO_x overlayers to be ≈4.6 Å.[56] The hydrated diameters of Cl^- and Br^- are larger by comparison at ≈6.5 Å,[78,105] suggesting that the full hydration shells would not fit within the SiO_x free volume elements and the ions would have to at least partially dehydrate to pass through.

If partial dehydration were a rate-limiting mechanism, Br^- would be expected to have a lower barrier to transport than Cl^- because Br^- has a larger electron shell radius and therefore a lower dehydration energy than Cl^-.[79] This expectation is consistent with our observation that P_{Br^-} is greater than P_{Cl^-}, warranting further consideration of a partial dehydration rate-limiting mechanism.

Mathematical models based on membrane transport theory can provide a more quantitative assessment of the differences in permeabilities that would result from a partial dehydration mechanism. In particular, an Arrhenius expression has been shown to be well suited for modeling species permeabilities through membrane materials with sub-nanometer pores or free

https://dx.doi.org/10.1021/acscatal.0c04343
ACS Catal. 2021, 11, 1316−1330

volume elements where partial dehydration limits transport[95] (eq 6)

$$P_i = A' \exp\left(-\frac{E_a}{RT}\right) \quad (6)$$

where P_i is the permeability of species i, A' is a pre-exponential frequency factor, E_a is the energy barrier for the rate-limiting transport step, R is the ideal gas constant, and T is the absolute temperature. In cases where partial dehydration is the transport-limiting step, E_a would correlate strongly with the dehydration energy of the ion.[98] Due to the exponential dependence of permeability on E_a in eq 6, a small difference in dehydration energy between Cl^- and Br^- could potentially lead to the observed 2-order-of-magnitude difference between the anions' permeabilities, in contrast with the more minor effect of hydrated ion radius on permeability. For example, if one assumes that two species have identical pre-exponential factors of $A' = 2 \times 10^{-7}$ cm^2 s^{-1}, similar to A' values derived from the literature,[90] our observed P_{Cl^-} and P_{Br^-} would correspond to E_a values of 31.8 and 23.7 kJ mol^{-1}, respectively, using eq 6 (Section XII, Supporting Information). For context, the enthalpy of hydration for Cl^- and Br^-, which is opposite in sign to the E_a theoretically required to fully dehydrate the ion, is −367 and −336 kJ mol^{-1}, respectively.[106] Since the energy barrier for partial dehydration is expected to be a fraction of the full dehydration energy,[93,107] our calculated E_a values are reasonable for a partial dehydration rate-limiting step.

Because the partial dehydration explanation aligns well with our preliminary empirical analysis, we posit that partial dehydration is a rate-limiting step for Cl^- transport through the SiO_x overlayers investigated in this work. Furthermore, partial dehydration could help explain the overlayer's selectivity for the OER over the CER since H_2O, the reactant for the OER, is the solvent within the aqueous electrolyte and is expected to have a much smaller activation barrier for crossing from the bulk electrolyte into the hydrophilic SiO_x overlayer. The most common water cluster sizes at pH 1, $(H_2O)_{1-6}$,[108] have full dissociation energies of less than 57 kJ mol^{-1},[109] suggesting that water's partial self-dehydration energy is far smaller than the partial dehydration energy of Cl^- and Br^-.

While the comparison of Cl^- and Br^- permeabilities appears to be consistent with partial ion dehydration playing a key role in determining relative transport rates, further work is needed to prove this hypothesis and address other unanswered questions related to transport mechanisms through ultrathin oxide coatings on electrodes. For example, the role of electromigration on species transport in ultrathin oxide coatings is generally unknown, as is the importance of stabilizing interactions between ions and electrode coatings.[96,110] Though the difference between P_{Cl^-} and P_{Br^-} can be described by realistic differences in partial dehydration E_a values computed based on an Arrhenius expression, differences in the pre-exponential factor in this relation could also account for the permeability differences. In distinct membrane transport cases, the A' value for Cl^- has been found to be orders of magnitude larger, orders smaller, or nearly identical to that of Br^-.[90,98,111] While no rate-limiting step considered here shows indication of creating a large difference in A' for SiO_x transport, such a difference may arise through poorly understood mechanisms such as electromigration or stabilizing interactions within the overlayer. Further experiments that expand to additional redox species with varying valency, size, and polarity, combined with operando structural characterization of the overlayers and atomistic simulations, are expected to be essential to further establishing design rules for selective oxide overlayers for seawater electrolysis.

3. CONCLUSIONS

This study has demonstrated that a catalytically inert SiO_x overlayer deposited on a planar Pt electrocatalyst can leverage selective transport properties of the overlayer to greatly suppress the CER while still permitting the desired OER to take place during electrolysis in a simulated acidic seawater environment. The ability of SiO_x overlayers to selectively block the CER is demonstrated in both acidic and pH-neutral environments that thermodynamically favor the CER, even at the high 0.6 M chloride concentration typical of seawater, at large CER overpotentials approaching 600 mV, and on a Pt electrocatalyst that is not particularly active for the OER. Based on mass transfer-limiting current densities, the SiO_x overlayers are characterized by a Cl^- permeability that is 3 orders of magnitude lower than that of a conventional reverse osmosis membrane. The chloride rejection of SiO_x overlayers could be further improved through optimization of the composition and structure of these overlayers, including possibly by incorporating anionic fixed charges into the overlayer to electrostatically repel Cl^-.

The overlayers also show robust stability in 12 h CA measurements at 1.55 V vs RHE, although some delamination becomes evident after a 12 h CA at a more positive potential of 1.90 V vs RHE. These instability issues are believed to be related to the formation of a PtO_x interlayer at the SiO_x|Pt buried interface on model thin film electrodes, suggesting that it should be possible to overcome this issue with alternative electrodes with optimized structure and composition that improves anchoring or avoids the formation of undesirable PtO_x interlayers. If the catalytic and adhesion properties of the buried interface can be improved while further enhancing the H_2O/Cl^- transport selectivity of overlayers, SiO_x-encapsulated electrocatalysts will offer an attractive means of achieving OER-selective seawater electrolysis without the added challenges of engineering electrolyte pH and mitigating chlorine corrosion.

4. EXPERIMENTAL SECTION

4.1. Electrode Fabrication. Monocrystalline degeneratively doped Si(100) wafers (p^+Si <0.005 Ω cm, 500−550 μm thick, WRS Materials) were used as conductive support substrates. To create the electrodes used in this study, thin films of Pt were deposited onto the p^+Si support with an adhesion layer of Ti in between the p^+Si and Pt. More specifically, thin films of 2 nm thick Ti (99.99%) and 3 nm thick Pt (99.99%) were sequentially deposited using electron-beam evaporation at 0.2 A s^{-1} without breaking vacuum and without substrate heating. Electron-beam evaporation was performed with a base pressure of 1.0×10^{-7} Torr in an Angstrom EvoVac evaporator system, with quartz crystal thickness monitors used to monitor film thicknesses. The Pt|Ti|p^+Si wafer was cleaved into 1.5 × 2 cm^2 pieces and then rinsed successively in acetone, methanol, isopropyl alcohol, and deionized water. Trimethylsiloxy-terminated poly(dimethylsiloxane) (PDMS) was spin-coated onto the Pt|Ti|p^+Si substrates at a speed of 4500 rpm for 2 min and 30 s using

https://dx.doi.org/10.1021/acscatal.0c04343
ACS Catal. 2021, 11, 1316−1330

four drops of PDMS/toluene solution that was deposited before spinning was initiated. PDMS in toluene concentrations of 1.2, 2.1, 3.0, 4.5, and 5.3 mg mL^{-1} were used to achieve SiO_x overlayer thicknesses of 1.2, 2.9, 4.8, 5.4, and 8.7 nm, respectively. The electrodes were then dried in an oven at atmospheric pressure at 90 °C for 60 min to evaporate the solvent. Afterward, the PDMS was converted to SiO_x in a UV−ozone cleaning chamber for 2 h (UVOCS, T10X10/OES). A low-resistance electrical back-contact was made by first scratching the back of the p^+Si substrate and then attaching a copper wire to the scratched area using indium solder. Finally, the electrodes were sealed in 3 M Electroplater's Tape to protect the back-contact and create a well-defined 0.26 cm^2 circular opening on the front of the electrode for electrochemical measurements.

4.2. Material Characterization. The thicknesses of the SiO_x films on the Pt|Ti|p^+Si substrates were measured using a Woollam alpha-SE ellipsometer and fit with a Cauchy model. Images of the electrodes were taken using a Zeiss Sigma VP Schottky thermal field emission scanning electron microscope (SEM). X-ray photoelectron spectroscopy (XPS) measurements were made with a Phi XPS system at pressures <2 $\times 10^{-10}$ Torr using a monochromatic Al Kα source (12.5 kV, 24 mA), with a pass energy of 23.5 eV, a step size of 0.05 eV, and a hold time of 200 ms. All samples were kept at 45° relative to the X-ray source. Si 2p and Pt 4f spectra were recorded, and analysis of the XPS data was performed as detailed elsewhere.[53] As previously reported, the as-deposited Pt thin films are characterized by rms roughness values <1 nm.[52] The fabrication method yielded a continuous, smooth SiO_x film of uniform thickness, as verified by atomic force microscopy (AFM) and ellipsometry measurements in previous studies.[52,53]

4.3. Electrochemical Measurements. Electrochemical measurements were performed at 25 °C in deaerated 0.5 M potassium bisulfate (+0.6 M potassium chloride) (+20 mM potassium bromide) prepared from potassium bisulfate salt ($KHSO_4$, reagent grade, Sigma-Aldrich), potassium chloride salt (KCl, anhydrous, Sigma-Aldrich), potassium bromide salt (KBr, anhydrous, Sigma-Aldrich), and 18 MΩ deionized water (Millipore, Milli-Q Direct 8). Unbuffered pH-neutral electrochemical measurements were performed in deaerated 0.1 M potassium nitrate and 0.6 M potassium chloride prepared from potassium nitrate salt (KNO_3, ACS reagent, Sigma-Aldrich), potassium chloride salt, and 18 MΩ deionized water. Additional measurements were performed in 0.5 M sulfuric acid + 0.6 M sodium chloride prepared from concentrated sulfuric acid (H_2SO_4, certified ACS plus, Fischer Scientific), sodium chloride salt (NaCl, anhydrous, Sigma-Aldrich), and 18 MΩ deionized water.

All electrochemical measurements were conducted with an SP-200 or SP-300 BioLogic potentiostat and carried out in a standard three-neck round-bottom glass cell with a commercial Ag|AgCl (3 M KCl) reference electrode (E 1/4 0.210 V vs NHE, Hach, E21M002) and a graphite rod counter electrode (Gamry). The electrolyte was stirred using a 3-inch-long magnetic stir bar at 200 rpm throughout all measurements. Newly made samples were used for each measurement. Immediately preceding each LSV or CA measurement, the existing Pt oxide at the Pt surface of the electrode was reduced to metallic Pt using three CV cycles between +0.04 and +0.94 V vs RHE.

■ ASSOCIATED CONTENT

Supporting Information

The Supporting Information is available free of charge at https://pubs.acs.org/doi/10.1021/acscatal.0c04343.

Electrochemical measurements in the supporting electrolyte of raised ionic density, time evolution of CV for 4.8 nm SiO_x|Pt in the saline electrolyte, LSV measurements for varied thickness SiO_x|Pt, 4.8 nm SiO_x|Pt LSV subtraction curve between the supporting and saline electrolytes, LSV measurements in neutral pH electrolytes, LSV measurements in the presence of 0.6 M NaCl, faradic efficiencies for OER, bromine evolution measurements for 4.8 nm SiO_x|Pt, and methods for calculation of P_{Br^-} and E_a (PDF)

■ AUTHOR INFORMATION

Corresponding Author

Daniel V. Esposito − *Department of Chemical Engineering, Columbia Electrochemical Engineering Center, Lenfest Center for Sustainable Energy, Columbia University in the City of New York, New York 10027, United States;* orcid.org/0000-0002-0550-801X; Email: de2300@columbia.edu

Authors

Amar A. Bhardwaj − *Department of Chemical Engineering, Columbia Electrochemical Engineering Center, Lenfest Center for Sustainable Energy, Columbia University in the City of New York, New York 10027, United States;* orcid.org/0000-0002-1082-7306

Johannes G. Vos − *Leiden Institute of Chemistry, Leiden University, 2300 RA Leiden, The Netherlands*

Marissa E. S. Beatty − *Department of Chemical Engineering, Columbia Electrochemical Engineering Center, Lenfest Center for Sustainable Energy, Columbia University in the City of New York, New York 10027, United States*

Amanda F. Baxter − *Department of Chemical Engineering, Columbia Electrochemical Engineering Center, Lenfest Center for Sustainable Energy, Columbia University in the City of New York, New York 10027, United States*

Marc T. M. Koper − *Leiden Institute of Chemistry, Leiden University, 2300 RA Leiden, The Netherlands*

Ngai Yin Yip − *Department of Earth and Environmental Engineering, Columbia Water Center, Columbia University in the City of New York, New York 10027, United States*

Complete contact information is available at: https://pubs.acs.org/10.1021/acscatal.0c04343

Notes

The authors declare the following competing financial interest(s): D.V.E. is a co-founder of sHYp, B.V.

■ ACKNOWLEDGMENTS

J.G.V. and M.T.M.K. acknowledge funding support from the Netherlands Organization for Scientific Research (NWO) in the framework of the fund New Chemical Innovations, project 731.015.204 ELECTROGAS, with financial support of Akzo Nobel Chemicals/Nouryon, Shell Global Solutions, Magneto Special Anodes (an Evoqua Brand), and Elson Technologies. A.A.B. acknowledges funding support from the Deresiewicz Research Fellowship, the Columbia University Materials Research Science and Engineering Center REU program, the Columbia Engineering Dean's Office Research Fellowship, and

the American Membrane Technology Association Fellowship. M.E.S.B. and D.V.E. acknowledge funding from the National Science Foundation (NSF) under Grant Number (CBET-1752340). D.V.E. and A.F.B. acknowledge funding support from the Qatar National Research Fund under its National Priorities Research Program award number NPRP12S-0131-190024 and co-funding from the Qatar Shell Research and Technology Center (QSRTC). Any opinions, findings, and conclusions or recommendations expressed in this material are those of the author(s) and do not necessarily reflect the views of the National Science Foundation.

REFERENCES

(1) Decker, G. L.; Gouse, W. S.; Gregory, D. P.; Hirsch, R. L.; Hoffman, K. C.; Hoos, I. R.; Johnson, J. E.; Longwell, J. P.; Siri, W. E.; Sliepcevich, C. M.; Smelt, R. *Hydrogen as a Fuel*; National Academies Press, 1979.

(2) Drab, D. M.; Willauer, H. D.; Olsen, M. T.; Ananth, R.; Mushrush, G. W.; Baldwin, J. W.; Hardy, D. R.; Williams, F. W. Hydrocarbon Synthesis from Carbon Dioxide and Hydrogen: A Two-Step Process. *Energy Fuels* **2013**, *27*, 6348−6354.

(3) Fukuzumi, S.; Lee, Y.-M.; Nam, W. Fuel Production from Seawater and Fuel Cells Using Seawater. *ChemSusChem* **2017**, *10*, 4264−4276.

(4) Jain, I. P. Hydrogen the Fuel for 21st Century. *Int. J. Hydrogen Energy* **2009**, *34*, 7368−7378.

(5) Dresp, S.; Dionigi, F.; Klingenhof, M.; Strasser, P. Direct Electrolytic Splitting of Seawater: Opportunities and Challenges. *ACS Energy Lett.* **2019**, *4*, 933−942.

(6) Urban, J. J. Emerging Scientific and Engineering Opportunities within the Water-Energy Nexus. *Joule* **2017**, *1*, 665−688.

(7) Dionigi, F.; Reier, T.; Pawolek, Z.; Gliech, M.; Strasser, P. Design Criteria, Operating Conditions, and Nickel-Iron Hydroxide Catalyst Materials for Selective Seawater Electrolysis. *ChemSusChem* **2016**, *9*, 962−972.

(8) Ahuja, K.; Mamtani, K. *Hypochlorite Bleaches Market Size by Product (Sodium Hypochlorite, Calcium Hypochlorite, Potassium Hypochlorite, Lithium Hypochlorite), by Application (Water Treatment, Textiles, Residential Pool Treatment, Laundry Bleaching, Disinfectants, Paper & Pulp), Industry Outlook Report, Regional Analysis, Application Potential, Price Trends, Competitive Market Share & Forecast, 2019−2025*; Global Market Insights, 2019.

(9) *Hydrogen Generation Market Size, Share & Trends Analysis Report by Application (Coal Gasification, Steam Methane Reforming), by Systems (Merchant, Captive), by Technology, and Segment Forecasts, 2020−2027*; Grand View Research, 2020.

(10) Chlorine Market by Production Method, by Application, by Industry Verticals (Pharmaceutical, Water Treatment, Paper & Pulp, Chemical, Plastic, and Others), and Segment Forecasts, 2016−2027; Reports and Data, 2019.

(11) Koper, M. T. M. Thermodynamic Theory of Multi-Electron Transfer Reactions: Implications for Electrocatalysis. *J. Electroanal. Chem.* **2011**, *660*, 254−260.

(12) Fujimura, K.; Izumiya, K.; Kawashima, A.; Akiyama, E.; Habazaki, H.; Kumagai, N.; Hashimoto, K. Anodically Deposited Manganese-Molybdenum Oxide Anodes with High Selectivity for Evolving Oxygen in Electrolysis of Seawater. *J. Appl. Electrochem.* **1999**, *29*, 765−771.

(13) Kuang, Y.; Kenney, M. J.; Meng, Y.; Hung, W. H.; Liu, Y.; Huang, J. E.; Prasanna, R.; Li, P.; Li, Y.; Wang, L.; Lin, M. C.; McGehee, M. D.; Sun, X.; Dai, H. Solar-Driven, Highly Sustained Splitting of Seawater into Hydrogen and Oxygen Fuels. *Proc. Natl. Acad. Sci. U.S.A.* **2019**, *116*, 6624−6629.

(14) Amikam, G.; Nativ, P.; Gendel, Y. Chlorine-Free Alkaline Seawater Electrolysis for Hydrogen Production. *Int. J. Hydrogen Energy* **2018**, *43*, 6504−6514.

(15) El-Moneim, A. A. Mn−Mo−W-Oxide Anodes for Oxygen Evolution During Seawater Electrolysis for Hydrogen Production: Effect of Repeated Anodic Deposition. *Int. J. Hydrogen Energy* **2011**, *36*, 13398−13406.

(16) Huang, W. H.; Lin, C. Y. Iron Phosphate Modified Calcium Iron Oxide as an Efficient and Robust Catalyst in Electrocatalyzing Oxygen Evolution from Seawater. *Faraday Discuss.* **2019**, *215*, 205−215.

(17) Yu, L.; Zhu, Q.; Song, S.; McElhenny, B.; Wang, D.; Wu, C.; Qin, Z.; Bao, J.; Yu, Y.; Chen, S.; Ren, Z. Non-Noble Metal-Nitride Based Electrocatalysts for High-Performance Alkaline Seawater Electrolysis. *Nat. Commun.* **2019**, *10*, No. 5106.

(18) Song, H. J.; Yoon, H.; Ju, B.; Lee, D.-Y.; Kim, D.-W. Electrocatalytic Selective Oxygen Evolution of Carbon-Coated Na2Co1−xFexP2O7 Nanoparticles for Alkaline Seawater Electrolysis. *ACS Catal.* **2020**, *10*, 702−709.

(19) Dresp, S.; Ngo Thanh, T.; Klingenhof, M.; Brückner, S.; Hauke, P.; Strasser, P. Efficient Direct Seawater Electrolysers Using Selective Alkaline NiFe-LDH As OER Catalyst in Asymmetric Electrolyte Feeds. *Energy Environ. Sci.* **2020**, 1725.

(20) Dresp, S.; Dionigi, F.; Loos, S.; Ferreira de Araujo, J.; Spöri, C.; Gliech, M.; Dau, H.; Strasser, P. Direct Electrolytic Splitting of Seawater: Activity, Selectivity, Degradation, and Recovery Studied from the Molecular Catalyst Structure to the Electrolyzer Cell Level. *Adv. Energy Mater.* **2018**, *8*, No. 1800338.

(21) Yu, L.; Wu, L.; McElhenny, B.; Song, S.; Luo, D.; Zhang, F.; Yu, Y.; Chen, S.; Ren, Z. Ultrafast Room-Temperature Synthesis of Porous S-Doped Ni/Fe (Oxy)Hydroxide Electrodes for Oxygen Evolution Catalysis in Seawater Splitting. *Energy Environ. Sci.* **2020**, *13*, 3439−3446.

(22) Đukić, A.; Firak, M. Hydrogen Production Using Alkaline Electrolyzer and Photovoltaic (PV) Module. *Int. J. Hydrogen Energy* **2011**, *36*, 7799−7806.

(23) Meier, K. Hydrogen Production with Sea Water Electrolysis Using Norwegian Offshore Wind Energy Potentials. *Int. J. Energy Environ. Eng.* **2014**, *5*, No. 104.

(24) d'Amore-Domenech, R.; Leo, T. J. Sustainable Hydrogen Production from Offshore Marine Renewable Farms: Techno-Energetic Insight on Seawater Electrolysis Technologies. *ACS Sustainable Chem. Eng.* **2019**, *7*, 8006−8022.

(25) Hessami, S.; Tobias, C. W. In-Situ Measurement of Interfacial pH Using a Rotating Ring-Disk Electrode. *AIChE J.* **1993**, *39*, 149−162.

(26) Snizhko, L. O.; Yerokhin, A. L.; Gurevina, N. L.; Patalakha, V. A.; Matthews, A. Excessive Oxygen Evolution During Plasma Electrolytic Oxidation of Aluminium. *Thin Solid Films* **2007**, *516*, 460−464.

(27) Tong, W.; Forster, M.; Dionigi, F.; Dresp, S.; Sadeghi Erami, R.; Strasser, P.; Cowan, A. J.; Farràs, P. Electrolysis of Low-Grade and Saline Surface Water. *Nat. Energy* **2020**, *5*, 367−377.

(28) Kadier, A.; Simayi, Y.; Abdeshahian, P.; Azman, N. F.; Chandrasekhar, K.; Kalil, M. S. A. Comprehensive Review of Microbial Electrolysis Cells (MEC) Reactor Designs and Configurations for Sustainable Hydrogen Gas Production. *Alexandria Eng. J.* **2016**, *55*, 427−443.

(29) Jwa, E.; Yun, Y.-M.; Kim, H.; Jeong, N.; Hwang, K. S.; Yang, S.; Nam, J.-Y. Energy-Efficient Seawater Softening and Power Generation Using a Microbial Electrolysis Cell-Reverse Electrodialysis Hybrid System. *Chem. Eng. J.* **2020**, *391*, No. 123480.

(30) McCrory, C. C.; Jung, S.; Ferrer, I. M.; Chatman, S. M.; Peters, J. C.; Jaramillo, T. F. Benchmarking Hydrogen Evolving Reaction and Oxygen Evolving Reaction Electrocatalysts for Solar Water Splitting Devices. *J. Am. Chem. Soc.* **2015**, *137*, 4347−4357.

(31) Petrykin, V.; Macounova, K.; Shlyakhtin, O. A.; Krtil, P. Tailoring the Selectivity for Electrocatalytic Oxygen Evolution on Ruthenium Oxides by Zinc Substitution. *Angew. Chem., Int. Ed.* **2010**, *49*, 4813−4815.

(32) Kato, Z.; Bhattarai, J.; Kumagai, N.; Izumiya, K.; Hashimoto, K. Durability Enhancement and Degradation of Oxygen Evolution Anodes in Seawater Electrolysis for Hydrogen Production. *Appl. Surf. Sci.* **2011**, *257*, 8230−8236.

https://dx.doi.org/10.1021/acscatal.0c04343
ACS Catal. 2021, 11, 1316−1330

(33) Kato, Z.; Sato, M.; Sasaki, Y.; Izumiya, K.; Kumagai, N.; Hashimoto, K. Electrochemical Characterization of Degradation of Oxygen Evolution Anode for Seawater Electrolysis. *Electrochim. Acta* **2014**, *116*, 152−157.
(34) El-Moneim, A. A.; Kumagai, N.; Asami, K.; Hashimoto, K. Nanocrystalline Manganese-Molybdenum-Tungsten Oxide Anodes for Oxygen Evolution in Acidic Seawater Electrolysis. *Mater. Trans.* **2005**, *46*, 309−316.
(35) Dinh, C.-T.; Jain, A.; de Arquer, F. P. G.; De Luna, P.; Li, J.; Wang, N.; Zheng, X.; Cai, J.; Gregory, B. Z.; Voznyy, O.; Zhang, B.; Liu, M.; Sinton, D.; Crumlin, E. J.; Sargent, E. H. Multi-Site Electrocatalysts for Hydrogen Evolution in Neutral Media by Destabilization of Water Molecules. *Nat. Energy* **2019**, *4*, 107−114.
(36) Esswein, A. J.; Surendranath, Y.; Reece, S. Y.; Nocera, D. G. Highly Active Cobalt Phosphate and Borate Based Oxygen Evolving Catalysts Operating in Neutral and Natural Waters. *Energy Environ. Sci.* **2011**, *4*, 499−504.
(37) Hsu, S. H.; Miao, J.; Zhang, L.; Gao, J.; Wang, H.; Tao, H.; Hung, S. F.; Vasileff, A.; Qiao, S. Z.; Liu, B. An Earth-Abundant Catalyst-Based Seawater Photoelectrolysis System with 17.9% Solar-to-Hydrogen Efficiency. *Adv. Mater.* **2018**, *30*, No. e1707261.
(38) Surendranath, Y.; Dinca, M.; Nocera, D. G. Electrolyte-Dependent Electrosynthesis and Activity of Cobalt-Based Water Oxidation Catalysts. *J. Am. Chem. Soc.* **2009**, *131*, 2615−2620.
(39) Carneiro-Neto, E. B.; Lopes, M. C.; Pereira, E. C. Simulation of Interfacial pH Changes During Hydrogen Evolution Reaction. *J. Electroanal. Chem.* **2016**, *765*, 92−99.
(40) Sharma, S. K. *Green Corrosion Chemistry and Engineering: Opportunities and Challenges*; Wiley-VCH Verlag GmbH & Co. KGaA: Weinheim, Germany, 2011.
(41) Bau, J. A.; Takanabe, K. Ultrathin Microporous SiO2 Membranes Photodeposited on Hydrogen Evolving Catalysts Enabling Overall Water Splitting. *ACS Catal.* **2017**, *7*, 7931−7940.
(42) Qureshi, M.; Shinagawa, T.; Tsiapis, N.; Takanabe, K. Exclusive Hydrogen Generation by Electrocatalysts Coated with an Amorphous Chromium-Based Layer Achieving Efficient Overall Water Splitting. *ACS Sustainable Chem. Eng.* **2017**, *5*, 8079−8088.
(43) Vos, J. G.; Wezendonk, T. A.; Jeremiasse, A. W.; Koper, M. T. M. MnOx/IrOx as Selective Oxygen Evolution Electrocatalyst in Acidic Chloride Solution. *J. Am. Chem. Soc.* **2018**, *140*, 10270−10281.
(44) Balaji, R.; Kannan, B. S.; Lakshmi, J.; Senthil, N.; Vasudevan, S.; Sozhan, G.; Shukla, A. K.; Ravichandran, S. An Alternative Approach to Selective Sea Water Oxidation for Hydrogen Production. *Electrochem. Commun.* **2009**, *11*, 1700−1702.
(45) Venkatkarthick, R.; Elamathi, S.; Sangeetha, D.; Balaji, R.; Suresh Kannan, B.; Vasudevan, S.; Jonas Davidson, D.; Sozhan, G.; Ravichandran, S. Studies on Polymer Modified Metal Oxide Anode for Oxygen Evolution Reaction in Saline Water. *J. Electroanal. Chem.* **2013**, *697*, 1−4.
(46) Garcia-Esparza, A. T.; Shinagawa, T.; Ould-Chikh, S.; Qureshi, M.; Peng, X.; Wei, N.; Anjum, D. H.; Clo, A.; Weng, T. C.; Nordlund, D.; Sokaras, D.; Kubota, J.; Domen, K.; Takanabe, K. An Oxygen-Insensitive Hydrogen Evolution Catalyst Coated by a Molybdenum-Based Layer for Overall Water Splitting. *Angew. Chem., Int. Ed.* **2017**, *56*, 5780−5784.
(47) Obata, K.; Takanabe, K. A Permselective CeOx Coating To Improve the Stability of Oxygen Evolution Electrocatalysts. *Angew. Chem., Int. Ed.* **2018**, *57*, 1616−1620.
(48) Vos, J. G.; Liu, Z.; Speck, F. D.; Perini, N.; Fu, W.; Cherevko, S.; Koper, M. T. M. Selectivity Trends Between Oxygen Evolution and Chlorine Evolution on Iridium-Based Double Perovskites in Acidic Media. *ACS Catal.* **2019**, *9*, 8561−8574.
(49) Huynh, M.; Bediako, D. K.; Nocera, D. G. A Functionally Stable Manganese Oxide Oxygen Evolution Catalyst in Acid. *J. Am. Chem. Soc.* **2014**, *136*, 6002−6010.
(50) Li, A.; Ooka, H.; Bonnet, N.; Hayashi, T.; Sun, Y.; Jiang, Q.; Li, C.; Han, H.; Nakamura, R. Stable Potential Windows for Long-Term Electrocatalysis by Manganese Oxides Under Acidic Conditions. *Angew. Chem., Int. Ed.* **2019**, *58*, 5054−5058.
(51) Ouyang, M.; Muisener, R. J.; Boulares, A.; Koberstein, J. T. UV−Ozone Induced Growth of a SiOx Surface Layer on a Cross-Linked Polysiloxane Film: Characterization and Gas Separation Properties. *J. Membr. Sci.* **2000**, *177*, 177−187.
(52) Beatty, M. E. S.; Chen, H.; Labrador, N. Y.; Lee, B. J.; Esposito, D. V. Structure−Property Relationships Describing the Buried Interface Between Silicon Oxide Overlayers and Electrocatalytic Platinum Thin Films. *J. Mater. Chem. A* **2018**, *6*, 22287−22300.
(53) Labrador, N. Y.; Songcuan, E. L.; De Silva, C.; Chen, H.; Kurdziel, S. J.; Ramachandran, R. K.; Detavernier, C.; Esposito, D. V. Hydrogen Evolution at the Buried Interface between Pt Thin Films and Silicon Oxide Nanomembranes. *ACS Catal.* **2018**, *8*, 1767−1778.
(54) Robinson, J. E.; Labrador, N. Y.; Chen, H.; Sartor, B. E.; Esposito, D. V. Silicon Oxide-Encapsulated Platinum Thin Films as Highly Active Electrocatalysts for Carbon Monoxide and Methanol Oxidation. *ACS Catal.* **2018**, *8*, 11423−11434.
(55) Pourbaix, M. *Atlas of Electrochemical Equilibria in Aqueous Solutions*; National Association of Corrosion Engineers: Houston, Texas, 1974.
(56) Beatty, M. E. S.; Gillette, E. I.; Haley, A. T.; Esposito, D. V. Controlling the Relative Fluxes of Protons and Oxygen to Electrocatalytic Buried Interfaces with Tunable Silicon Oxide Overlayers. *ACS Appl. Energy Mater.* **2020**, *3* (12), 12338−12350.
(57) Yuan, G.; Agiral, A.; Pellet, N.; Kim, W.; Frei, H. Inorganic Core-Shell Assemblies for Closing the Artificial Photosynthetic Cycle. *Faraday Discuss.* **2014**, *176*, 233−249.
(58) Conway, B. E. Electrochemical Oxide Film Formation at Noble Metals as a Surface-Chemical Process. *Prog. Surf. Sci.* **1995**, *49*, 331−452.
(59) Conway, B. E.; Mozota, J., Chloride-ion Effects on the Reversible and Irreversible Surface Oxidation Processes at Pt Electrodes, and on the Growth of Monolayer Oxide Films at Pt. *J. Chem. Soc., Faraday Trans. 1* **1982**, *78*, DOI: 10.1039/f19827801717.
(60) Kolics, A.; Wieckowski, A. Adsorption of Bisulfate and Sulfate Anions on a Pt(111) Electrode. *J. Phys. Chem. B* **2001**, *105*, 2588−2595.
(61) Harvey, H. W. The Chemistry and Fertility of Sea Waters. *J. Mar. Biol. Assoc. U.K.* **1956**, *35*, 289.
(62) Novak, D. M.; Conway, B. E. Competitive Adsorption and State of Charge of Halide Ions in Monolayer Oxide Film Growth Processes at Pt Anodes. *J. Chem. Soc., Faraday Trans. 1* **1981**, *77*, 2341.
(63) Pavlišič, A.; Jovanovic, P.; Selih, V. S.; Sala, M.; Hodnik, N.; Hocevar, S.; Gaberscek, M. The Influence of Chloride Impurities on Pt/C Fuel Cell Catalyst Corrosion. *Chem. Commun.* **2014**, *50*, 3732−3734.
(64) Real, S. G.; Barbosa, M. R.; Vilche, J. R.; Arvia, A. J. Influence of Chloride Concentration on the Active Dissolution and Passivation of Nickel Electrodes in Acid Sulfate Solutions. *J. Electrochem. Soc.* **1990**, *137*, 1696.
(65) Tsuru, T. Anodic Dissolution Mechanisms of Metals and Alloys. *Mater. Sci. Eng., A* **1991**, *146*, 1−14.
(66) Jung, H.; Alfantazi, A. Corrosion Properties of Electrodeposited Cobalt in Sulfate Solutions Containing Chloride Ions. *Electrochim. Acta* **2010**, *55*, 865−869.
(67) Moreno-Hernandez, I. A.; Brunschwig, B. S.; Lewis, N. S. Crystalline Nickel, Cobalt, and Manganese Antimonates as Electrocatalysts for the Chlorine Evolution Reaction. *Energy Environ. Sci.* **2019**, *12*, 1241−1248.
(68) Lobo, V. M. M.; Ribeiro, A. C. F.; Verissimo, L. M. P. Diffusion Coefficients in Aqueous Solutions of Potassium Chloride at High and Low Concentrations. *J. Mol. Liq.* **1998**, *78*, 139−149.
(69) Ohya, H.; Semenova, S.; Mizoguchi, K.; Ogihara, J.; Fukaya, S.; Suzuki, Y.; Aihara, M.; Negishi, Y. Distribution and Diffusion Coefficients of NaCl in Polyamide (Nylon-6,6 and Polyxylyleneadipamide) Membranes. *J. Appl. Polym. Sci.* **2002**, *84*, 2605−2612.
(70) Ren, H.; German, S. R.; Edwards, M. A.; Chen, Q.; White, H. S. Electrochemical Generation of Individual O2 Nanobubbles via H2O2 Oxidation. *J. Phys. Chem. Lett.* **2017**, *8*, 2450−2454.

(71) Gottesfeld, S.; Maia, G.; Floriano, J. B.; Tremilioso-Filho, G.; Ticianelli, E. A.; Gonzalez, E. R. Study of Thick Anodic Oxide Films on Pt by Spectroscopic Ellipsometry. *J. Electrochem. Soc.* **1991**, *138*, 3219−3224.
(72) Miles, M. H.; Klaus, E. A.; Gunn, B. P.; Locker, J. R.; Serafin, W. E.; Srinivasan, S. The Oxygen Evolution Reaction on Platinum, Iridium, Ruthenium and Their Alloys at 80 °C in Acid Solutions. *Electrochim. Acta* **1978**, *23*, 521−526.
(73) Roscoe, S. G.; Conway, B. E. State Of Surface Oxide Films at Pt Anodes and "Volcano" Behaviour in Electrocatalysis for Anodic Cl_2 Evolution. *J. Electroanal. Chem. Interfacial Electrochem.* **1987**, *224*, 163−188.
(74) Takenaka, S.; Miyamoto, H.; Utsunomiya, Y.; Matsune, H.; Kishida, M. Catalytic Activity of Highly Durable Pt/CNT Catalysts Covered with Hydrophobic Silica Layers for the Oxygen Reduction Reaction in PEFCs. *J. Phys. Chem. C* **2014**, *118*, 774−783.
(75) Takenaka, S.; Miyazaki, T.; Matsune, H.; Kishida, M. Highly Active and Durable Silica-Coated Pt Cathode Catalysts for Polymer Electrolyte Fuel Cells: Control of Micropore Structures in Silica Layers. *Catal. Sci. Technol.* **2015**, *5*, 1133−1142.
(76) Jo, W. J.; Katsoukis, G.; Frei, H. Ultrathin Amorphous Silica Membrane Enhances Proton Transfer Across Solid-to-Solid Interfaces of Stacked Metal Oxide Nanolayers While Blocking Oxygen. *Adv. Funct. Mater.* **2020**, *30*, No. 1909262.
(77) Israelachvili, J. N. Interactions Involving Polar Molecules. *Intermolecular and Surface Forces*; Academic Press, 2011; pp 71−90.
(78) Nightingale, E. R., Jr. Phenomenological Theory of Ion Solvation: Effective Radii of Hydrated Ions. *J. Phys. Chem. A* **1959**, *63*, 1381−1387.
(79) Fawcett, R. W. Thermodynamic Parameters for the Solvation of Monatomic Ions in Water. *J. Phys. Chem. B* **1999**, *103*, 11181−11185.
(80) O'Hern, S. C.; Boutilier, M. S.; Idrobo, J. C.; Song, Y.; Kong, J.; Laoui, T.; Atieh, M.; Karnik, R. Selective Ionic Transport through Tunable Subnanometer Pores in Single-Layer Graphene Membranes. *Nano Lett.* **2014**, *14*, 1234−1241.
(81) Zhang, C.; Lively, R. P.; Zhang, K.; Johnson, J. R.; Karvan, O.; Koros, W. J. Unexpected Molecular Sieving Properties of Zeolitic Imidazolate Framework-8. *J. Phys. Chem. Lett.* **2012**, *3*, 2130−2134.
(82) Mi, B. Graphene Oxide Membranes for Ionic and Molecular Sieving. *Science* **2014**, *343*, 740−742.
(83) Deng, M.; Kwac, K.; Li, M.; Jung, Y.; Park, H. G. Stability, Molecular Sieving, and Ion Diffusion Selectivity of a Lamellar Membrane from Two-Dimensional Molybdenum Disulfide. *Nano Lett.* **2017**, *17*, 2342−2348.
(84) Labrador, N. Y.; Li, X.; Liu, Y.; Tan, H.; Wang, R.; Koberstein, J. T.; Moffat, T. P.; Esposito, D. V. Enhanced Performance of Si MIS Photocathodes Containing Oxide-Coated Nanoparticle Electrocatalysts. *Nano Lett.* **2016**, *16*, 6452−6459.
(85) Atkins, P.; De Paula, J. *Physical Chemistry*, 8th ed.; Oxford University Press: Oxford, 2006.
(86) Zhang, H.; Hou, J.; Hu, Y.; Wang, P.; Ou, R.; Jiang, L.; Liu, J. Z.; Freeman, B. D.; Hill, A. J.; Wang, H. Ultrafast Selective Transport of Alkali Metal Ions in Metal Organic Frameworks with Subnanometer Pores. *Sci. Adv.* **2018**, *4*, No. eaaq0066.
(87) Gao, L.; Chan, K. Y.; Li, C. V.; Xie, L.; Olorunyomi, J. F. Highly Selective Transport of Alkali Metal Ions by Nanochannels of Polyelectrolyte Threaded MIL-53 Metal Organic Framework. *Nano Lett.* **2019**, *19*, 4990−4996.
(88) Wang, G.; Zhang, B.; Wayment, J. R.; Harris, J. M.; White, H. S. Electrostatic-Gated Transport in Chemically Modified Glass Nanopore Electrodes. *J. Am. Chem. Soc.* **2006**, *128*, 7679−7686.
(89) Kim, Y.-J.; Choi, J.-H. Enhanced Desalination Efficiency in Capacitive Deionization with an Ion-Selective Membrane. *Sep. Purif. Technol.* **2010**, *71*, 70−75.
(90) Epsztein, R.; Shaulsky, E.; Dizge, N.; Warsinger, D. M.; Elimelech, M. Role of Ionic Charge Density in Donnan Exclusion of Monovalent Anions by Nanofiltration. *Environ. Sci. Technol.* **2018**, *52*, 4108−4116.
(91) Ishii, Y.; Kobayashi, Y.; Watanabe, K.-i.; Koda, H.; Kunigami, H.; Kunigami, H. Fabrication of Silica/Platinum Core-Shell Particles by Electroless Metal Plating. *Adv. Powder Technol.* **2019**, *30*, 829−834.
(92) Cloarec, J. P.; Chevalier, C.; Genest, J.; Beauvais, J.; Chamas, H.; Chevolot, Y.; Baron, T.; Souifi, A. pH Driven Addressing of Silicon Nanowires onto Si3N4/SiO2 Micro-Patterned Surfaces. *Nanotechnology* **2016**, *27*, No. 295602.
(93) Richards, L. A.; Schafer, A. I.; Richards, B. S.; Corry, B. The Importance of Dehydration in Determining Ion Transport in Narrow Pores. *Small* **2012**, *8*, 1701−1709.
(94) Sahu, S.; Di Ventra, M.; Zwolak, M. Dehydration as a Universal Mechanism for Ion Selectivity in Graphene and Other Atomically Thin Pores. *Nano Lett.* **2017**, *17*, 4719−4724.
(95) Epsztein, R.; DuChanois, R. M.; Ritt, C. L.; Noy, A.; Elimelech, M. Towards Single-Species Selectivity of Membranes with Subnanometre Pores. *Nat. Nanotechnol.* **2020**, *15*, 426−436.
(96) Gouaux, E.; MacKinnon, R. Principles of Selective Ion Transport in Channels and Pumps. *Science* **2005**, *310*, 1461−1465.
(97) Sun, P.; Zheng, F.; Zhu, M.; Song, Z.; Wang, K.; Zhong, M.; Wu, D.; Little, R. B.; Xu, Z.; Zhu, H. Selective Trans-Membrane Transport of Alkali and Alkaline Earth Cations through Graphene Oxide Membranes Based on Cation-π Interactions. *ACS Nano* **2014**, *8*, 850−859.
(98) Epsztein, R.; Shaulsky, E.; Qin, M.; Elimelech, M. Activation Behavior for Ion Permeation in Ion-Exchange Membranes: Role of Ion Dehydration in Selective Transport. *J. Membr. Sci.* **2019**, *580*, 316−326.
(99) Richards, L. A.; Schafer, A. I.; Richards, B. S.; Corry, B. Quantifying Barriers to Monovalent Anion Transport in Narrow Non-Polar Pores. *Phys. Chem. Chem. Phys.* **2012**, *14*, 11633−11638.
(100) Sigurdardottir, S. B.; DuChanois, R. M.; Epsztein, R.; Pinelo, M.; Elimelech, M. Energy Barriers to Anion Transport in Polyelectrolyte Multilayer Nanofiltration Membranes: Role of Intra-Pore Diffusion. *J. Membr. Sci.* **2020**, *603*, No. 117921.
(101) Tansel, B. Significance of Thermodynamic and Physical Characteristics on Permeation of Ions During Membrane Separation: Hydrated Radius, Hydration Free Energy and Viscous Effects. *Sep. Purif. Technol.* **2012**, *86*, 119−126.
(102) Zwolak, M.; Wilson, J.; Di Ventra, M. Dehydration and Ionic Conductance Quantization in Nanopores. *J. Phys.: Condens. Matter* **2010**, *22*, No. 454126.
(103) Jain, T.; Rasera, B. C.; Guerrero, R. J.; Boutilier, M. S.; O'Hern, S. C.; Idrobo, J. C.; Karnik, R. Heterogeneous Sub-Continuum Ionic Transport in Statistically Isolated Graphene Nanopores. *Nat. Nanotechnol.* **2015**, *10*, 1053−1057.
(104) Wang, M.; Shen, W.; Ding, S.; Wang, X.; Wang, Z.; Wang, Y.; Liu, F. A Coupled Effect of Dehydration and Electrostatic Interactions on Selective Ion Transport through Charged Nanochannels. *Nanoscale* **2018**, *10*, 18821−18828.
(105) Marcus, Y. Ionic Radii in Aqueous Solutions. *Chem. Rev.* **1988**, *88*, 1475−1498.
(106) Marcus, Y. The Thermodynamics of Solvation of Ions Part 2.—The Enthalpy of Hydration at 298.15 K. *J. Chem. Soc., Faraday Trans. 1* **1987**, *83*, 339−349.
(107) Song, C.; Corry, B. Intrinsic Ion Selectivity of Narrow Hydrophobic Pores. *J. Phys. Chem. B* **2009**, *113*, 7642−7649.
(108) Liu, Y.-Y.; Hua, X.; Zhang, Z.; Zhang, J.; Zhang, S.; Hu, P.; Long, Y.-T. pH-Dependent Water Clusters in Photoacid Solution: Real-Time Observation by ToF-SIMS at a Submicropore Confined Liquid-Vacuum Interface. *Front. Chem.* **2020**, *8*, No. 731.
(109) Liu, X.; Lu, W.-C.; Wang, C. Z.; Ho, K. M. Energetic and Fragmentation Stability of Water Clusters (H2O)n, n=2−30. *Chem. Phys. Lett.* **2011**, *508*, 270−275.
(110) Li, X.; Zhang, H.; Wang, P.; Hou, J.; Lu, J.; Easton, C. D.; Zhang, X.; Hill, M. R.; Thornton, A. W.; Liu, J. Z.; Freeman, B. D.; Hill, A. J.; Jiang, L.; Wang, H. Fast and Selective Fluoride Ion Conduction in Sub-1-Nanometer Metal-Organic Framework Channels. *Nat. Commun.* **2019**, *10*, No. 2490.

https://dx.doi.org/10.1021/acscatal.0c04343
ACS Catal. 2021, 11, 1316−1330

(111) Dalmark, M.; Wieth, J. O. Temperature Dependence of Chloride, Bromide, Iodide, Thiocyanate and Salicylate Transport in Human Red Cells. *J. Physiol.* **1972**, *224*, 583−610.

https://dx.doi.org/10.1021/acscatal.0c04343
ACS Catal. 2021, 11, 1316−1330